Storms, Variability, and Multiple Equilibria on Hot Jupiters

James Y-K. Cho[1] ⬛, Jack W. Skinner[2] ⬛, and Heidar Th. Thrastarson[3] ⬛
[1] CCA, Flatiron Institute, New York, NY 10010, USA; jcho@flatironinstitute.org
[2] School of Physics and Astronomy, Queen Mary University of London, London E1 4NS, UK
[3] Jet Propulsion Laboratory, California Institute of Technology, Pasadena, CA 91109, USA

Abstract

Observations of hot-Jupiter atmospheres show large variations in the location of the "hot spot" and the amplitude of spectral features. Atmospheric flow simulations using the commonly employed forcing and initialization have generally produced a large, monolithic patch of nearly stationary hot area located eastward of the substellar point at high altitude. Here we perform high-resolution (T682) pseudospectral simulations that accurately capture small-scale eddies and waves inherent in hot-Jupiter atmospheres due to ageostrophy. The atmospheres contain a large number of intense storms over a wide range of scales, including the planetary scale. The latter sized storms dictate the large-scale spatial distribution and temporal variability of hot, as well as cold, regions over the planet. In addition, they exhibit quasi-periodic life cycles within multiple equilibrium states—all identifiable in the disk-integrated time series of the temperature flux.

1. Introduction

Hot Jupiters orbit very close to their host stars. Therefore, they are expected to be in a 1:1 spin–orbit synchronized state and possess a high likelihood of transiting their host stars. Consequently, hot-Jupiter atmospheres are hitherto the best observed of all the extrasolar planet atmospheres (e.g., Knutson et al. 2007; Grillmair et al. 2008; Swain et al. 2008; Crossfield et al. 2010; Armstrong et al. 2016; Bell et al. 2019; Jackson et al. 2019; von Essen et al. 2019). Such observations represent the first step toward assessing weather and climate on extrasolar planets. However, to reliably interpret and to optimally plan observations, accurate knowledge of the three-dimensional (3D), global atmospheric flow and temperature patterns is crucial. A major reason for this is because dynamics forms the backbone for accurate modeling of all the other important atmospheric processes (e.g., radiative transfer, clouds, photochemistry, and ionization).

Objects that are 1:1 spin–orbit synchronized are heated only on one side, the "dayside." Such thermal forcing leads to global flow and temperature patterns that are markedly different than those of the solar system planets. Thus far, simulations have either lacked the required horizontal resolution or have been barotropic—i.e., two-dimensional (2D; e.g., Showman & Guillot 2002; Cho et al. 2003, 2008; Showman et al. 2009; Rauscher & Menou 2010; Thrastarson & Cho 2010; Heng et al. 2011; Dobbs-Dixon & Agol 2013; Liu & Showman 2013; Mayne et al. 2014; Polichtchouk et al. 2014; Mendonça et al. 2016; Penn & Vallis 2017; Komacek & Showman 2020; Menou 2020). Hence, they have not been able to accurately capture the dynamics of small scales, important for the nonlinear interactions with large scales, and/or the crucial vertical coupling and variations (Cho et al. 2003; Watkins & Cho 2010; Thrastarson & Cho 2011; Polichtchouk & Cho 2012; Cho et al. 2015; Skinner & Cho 2021a, 2021b). In this Letter, we report on the results from a series of high-resolution, 3D simulations using a highly accurate and well-tested pseudospectral code for extrasolar planets (Polichtchouk et al. 2014; Cho et al. 2015; Skinner & Cho 2021a). The code solves the traditional primitive equations (e.g., Polichtchouk et al. 2014) with a high-order hyperviscosity (e.g., Cho & Polvani 1996).

2. Setup

We employ an idealized setup that is commonly used in extrasolar planet atmosphere modeling to generate the flow and temperature distributions starting from an initial resting state (e.g., Liu & Showman 2013; Cho et al. 2015); see also Skinner & Cho (2021a, 2021b) for all the physical and numerical parameters and values belonging to the simulations presented in this Letter. The setup consists of "relaxing" the temperature field of the flow to a prescribed equilibrium temperature distribution on a specified timescale at different pressure levels. Although highly idealized, this is a reasonable and practical first representation of the thermal forcing in the absence of detailed information—if the temperature perturbations from the mean are not too large (Cho et al. 2008). However, hot extrasolar planet atmospheres can possess large temperature perturbations and are typically in a highly ageostrophic regime, out of pressure gradient and Coriolis acceleration balance (Cho et al. 2015). This is because the rotation period τ of the planet is generally not short and the gravity wave speed c in the atmosphere is very fast (e.g., $\tau \approx 3.025 \times 10^5$ s and $c \sim 2.7 \times 10^3$ m s^{-1} for the planet described in this Letter). In this situation, the setup requires a very high resolution and stability for accurate simulations.

3. Results

Figure 1 shows the flow field (relative vorticity ζ from a T682L20 resolution simulation with ∇^{16} hyperviscosity. Here "T682L20" refers to 682 total wavenumbers and 682 zonal wavenumbers in the spherical harmonics for each of the 20
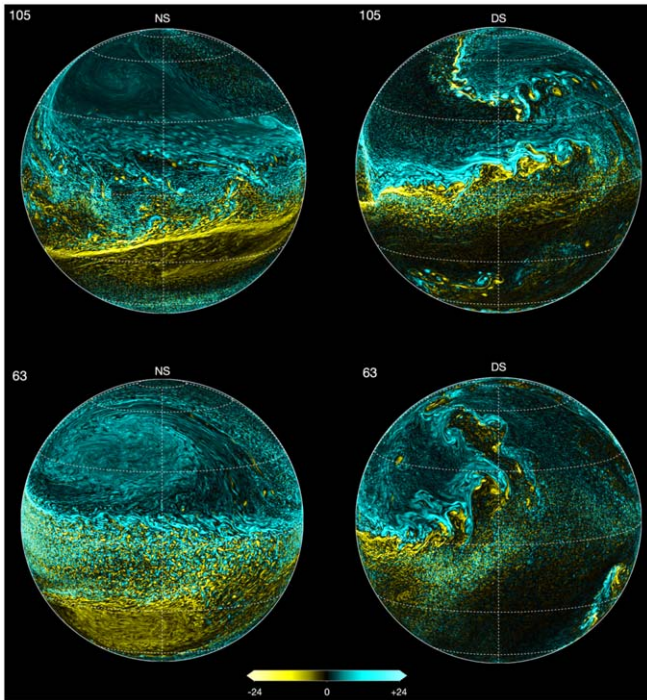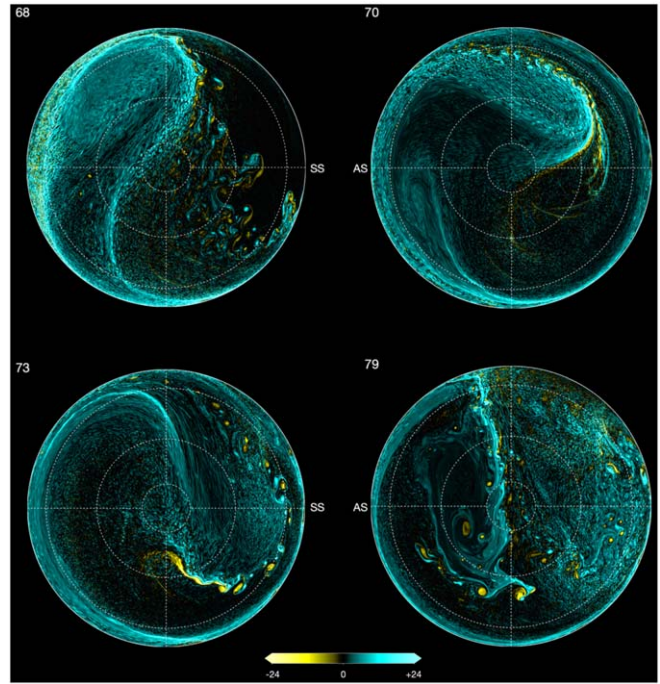
Figure 1. Relative vorticity field ζ, showing intense storms and meandering jet streams. The pressure levels are 0.005 MPa (top row) and 0.095 MPa (bottom row); the time (in the unit of a planetary rotation τ) is indicated at the upper left of each frame. The nightside (NS) and dayside (DS) fields are shown centered on the antistellar and substellar points, respectively. Cyan and yellow colors correspond to regions of $\zeta > 0$ and $\zeta < 0$, respectively, in the unit of $2\pi/\tau$. Highly dynamic storms form over a wide range of scales. The planetary-scale storms exhibit quasi-periodic life cycles.

pressure levels of the computational domain (Skinner & Cho 2021a). With the above viscosity, the resolution corresponds to effectively at least an order of magnitude higher resolution in the horizontal direction than those of past 3D simulations with comparable vertical resolution (e.g., Menou 2020). In other simulations discussed in this work (T341L200), the vertical resolution is also two orders of magnitude higher than those of past 2D hot-Jupiter simulations with comparable horizontal resolution (e.g., Cho et al. 2003). The fields from near the top and bottom of the T682L20 simulation are shown.[4] Time t is in the unit of τ.

Several features are immediately apparent. First, the flow is extremely dynamic, and this characteristic persists over the entire duration of the simulation (300 τ here and 2000 τ in the T341L200 simulations). The dynamism here is crucial because it actively redistributes temperature as well as radiatively and chemically important species across the face of the planet. Such spatiotemporal variability caused by evolving storms on a close-in planet was first shown by Cho et al. (2003) in their 2D simulations employing T341 resolution with ∇^{16} hyperviscosity. Second, the flow contains a very large number of intense storms over the full range of scales—from the planetary scale down to nearly the dissipation-scale (near the scale of the truncation wavenumber in the spherical harmonics. At the


Figure 2. The twilight phase of a cyclonic modon, in which the modon is ultimately replaced by a polar vortex. The ζ field at the 0.005 MPa level from the simulation of Figure 1 is shown, viewed from the north: the phase occurs in both hemispheres. In each frame, the substellar point (SS), antistellar point (AS), eastern terminator, and western terminator are at the right, left, top, and bottom, respectively. Planetary-scale storms spawn and then disperse smaller storms across the face of the planet.

planetary scale, there are two modons[5]: one comprising a pair of cyclones—e.g., at $t = 63$ nightside (NS)—and the other a (generally weaker) pair of anticyclones.[6] Third, concurrent with the modons are sharp fronts and high-speed jets that break and continuously spawn medium- and small-scale storms. The modons also directly generate energetic, small-scale gravity waves (Watkins & Cho 2010) and storms as they attempt to adjust in the ageostrophic environment (Lahaye & Zeitlin 2012). Finally, the modons are also important in blocking equatorial jets, breaking the zonal symmetry suggested in many past simulations (e.g., Showman & Polvani 2011; Liu & Showman 2013; Menou 2020). These features—as well as others discussed below—are independent of the location of the bottom of the domain (from 0.1 MPa to 20 MPa), provided the vertical range modeled is well resolved with an adequate number of levels.

Medium- and small-scale storms form and move across hot-Jupiter atmospheres by many different mechanisms (Cho et al. 2003, 2008; Thrastarson & Cho 2010; Watkins & Cho 2010; Polichtchouk & Cho 2012; Tsai et al. 2014; Cho et al. 2015; Fromang et al. 2016). These storms are important because they assist planetary-scale storms in chaotically mixing the atmosphere on the global scale. Figure 2 shows a prominent, *recurring* mechanism—nonlinear breaking and advection by a modon. At $t = 68$, a large cyclonic modon that initially formed just to the west of the substellar (SS) point has traversed across the nightside and reached the eastern terminator (ET; top of the

---

[4] The domain of this simulation extends down to 0.1 MPa. The 0.1 MPa level is traditionally where the radius of a giant planet R_p ($= 10^8$ m, for the planet of this Letter) is measured and where most of the visible irradiation is expected to be fully absorbed on a hot Jupiter (e.g., Seager et al. 2005). The proper location of the bottom (or the top) for simulations is currently unknown (Cho et al. 2008).

[5] A modon is a long-lived, coherent pair of storms (a vortex couple) with opposite signs of ζ (Stern 1975).

[6] Cyclones (anticyclones) are vortical structures that spin in the same (opposite) direction as the planet's north direction.
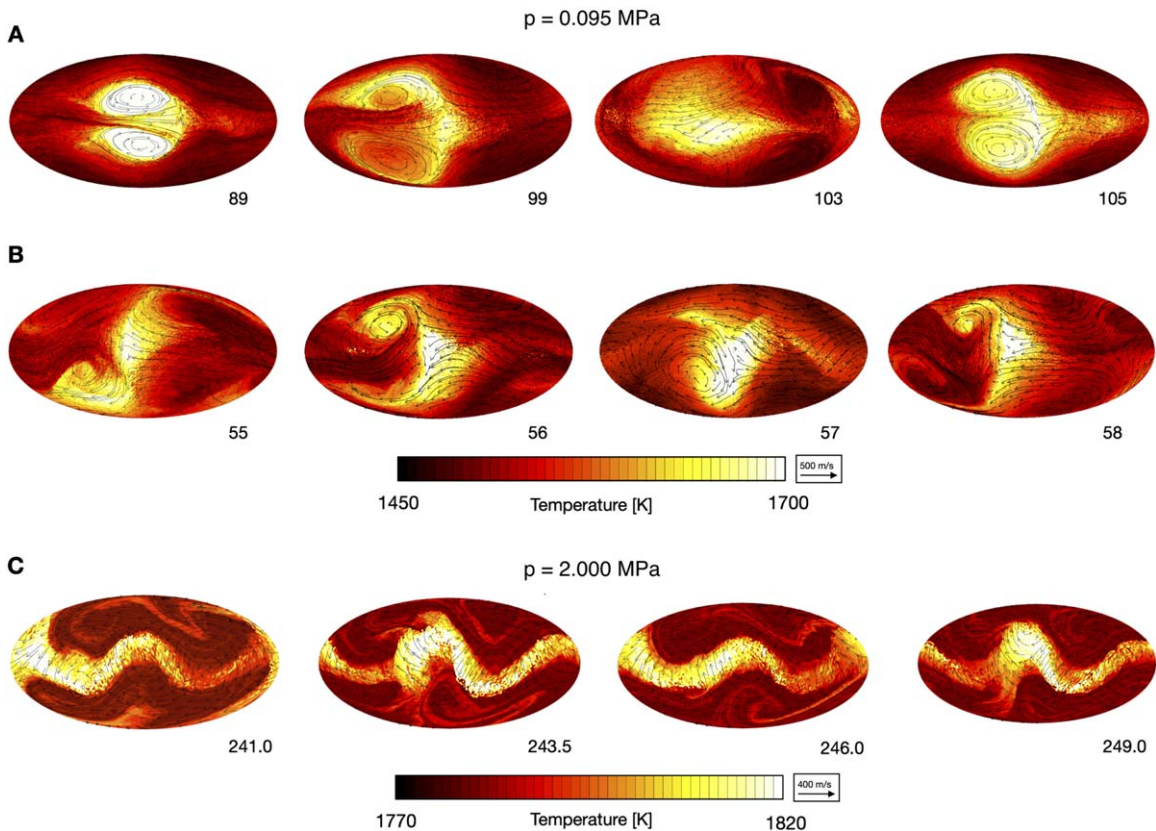
Figure 3. Spatiotemporal variability in the temperature field T. The fields at the 0.095 MPa (A and B) and the 2.000 MPa (C) levels in Mollweide projection, centered at the SS point, are shown with time indicated at the lower right of each frame. Velocity vectors show the close association of the flow and T fields. The frames in (A) and (B) are from a T341L20 simulation, and the frames in (C) are from a T341L200 simulation. Regardless of the domain range, different variability states exist at the same level (A and B) as well as at different levels (A and C). The variability is much more regular and wave-like in (C), compared with those in (A) and (B), but the thermal wave is highly nonlinear and periodically steepens, inducing elevated temperatures at different longitudes and latitudes at different times. Modons initially form near the SS and AS points, sequester hot and cold masses of air, and then transport and mix the masses across the planet quasi-periodically as they move.

frame). Throughout the traversal, the boundary of the modon continuously breaks and rolls up into many storms. At $t = 70$, the modon has moved past the terminator, to a higher latitude, generating sharp fronts ahead (in longitude) and below (in latitude); at this point, the northern half of the modon also begins to separate from its partner cyclone in the southern hemisphere. Here one can also see gravity waves ahead of, and above, the modon—as well as a second cyclone forming downstream, near the antistellar (AS) point. By $t = 73$, the modon has passed over the SS point and intense storms generated at the periphery of the modon are dispersed widely across the dayside, from the low- to mid-latitudes. Thereafter, the modon dissipates and is replaced (in this cycle) by a planetary-scale vortex of nearly uniform ζ near the pole, at $t = 79$; note also the "next-generation" cyclonic modon, brewing near the SS point at this time. The overall motion of the modon, and its induced long-range motion, is chaotic and not smooth from its inception, but it is quasi-periodic.

In Figure 3, we illustrate several quasi-periodic patterns of temperature field T induced by the modons. There are more patterns than presented. The frames in Figures 3(A) and (B) are from a T341L20 simulation in which the pressure range of the domain is [0, 0.1] MPa. The frames in Figure 3(C) are from a T341L200 simulation in which the pressure range of the domain is [0, 10] MPa. The behaviors at the 0.095 MPa level shown are qualitatively similar in both simulations (as well as in the T682L20 simulation above), albeit at different pressure

levels. The T341L200 simulation is not level-wise converged with the T341L20 and T682L20 simulations because higher resolution (vertical and horizontal) is required and the baroclinic structure of the flow is slghtly different (Skinner & Cho 2021a, 2021b).[7] In the figure, the velocity vectors are overlaid on the T field and show the close relationship between the flow and temperature. In particular, modons sequester hot and cold air masses and redistribute them over long distances.

For example, without the cyclonic modon (as well as other structures, such as fronts, associated with strong flows), the T field at $t = 89$ in Figure 3(A) would be a circular patch of "hot spot" centered at the SS point (instead of two disjointed patches) without the cyclonic modon (or other structures associated with strong flows); similarly, without the anticyclonic modon, the T field would be a single cold patch centered at the AS point, rather than two separate cold patches at high latitudes. As the modons move (westward at $t = 99$), they transport large patches of hot and cold air; both modons move and mix in both types of air. Note here that the hottest region is well west of the SS point. At $t = 103$, the anticyclonic modon (now in the western hemisphere) has split apart, each half moving toward its respective pole; here the anticyclones heat the polar regions as they move. Simultaneously, the intense cyclonic modon just emerging from the nightside at the

---

[7] The flows in all three simulations are still predominantly barotropic (i.e., vertically aligned).
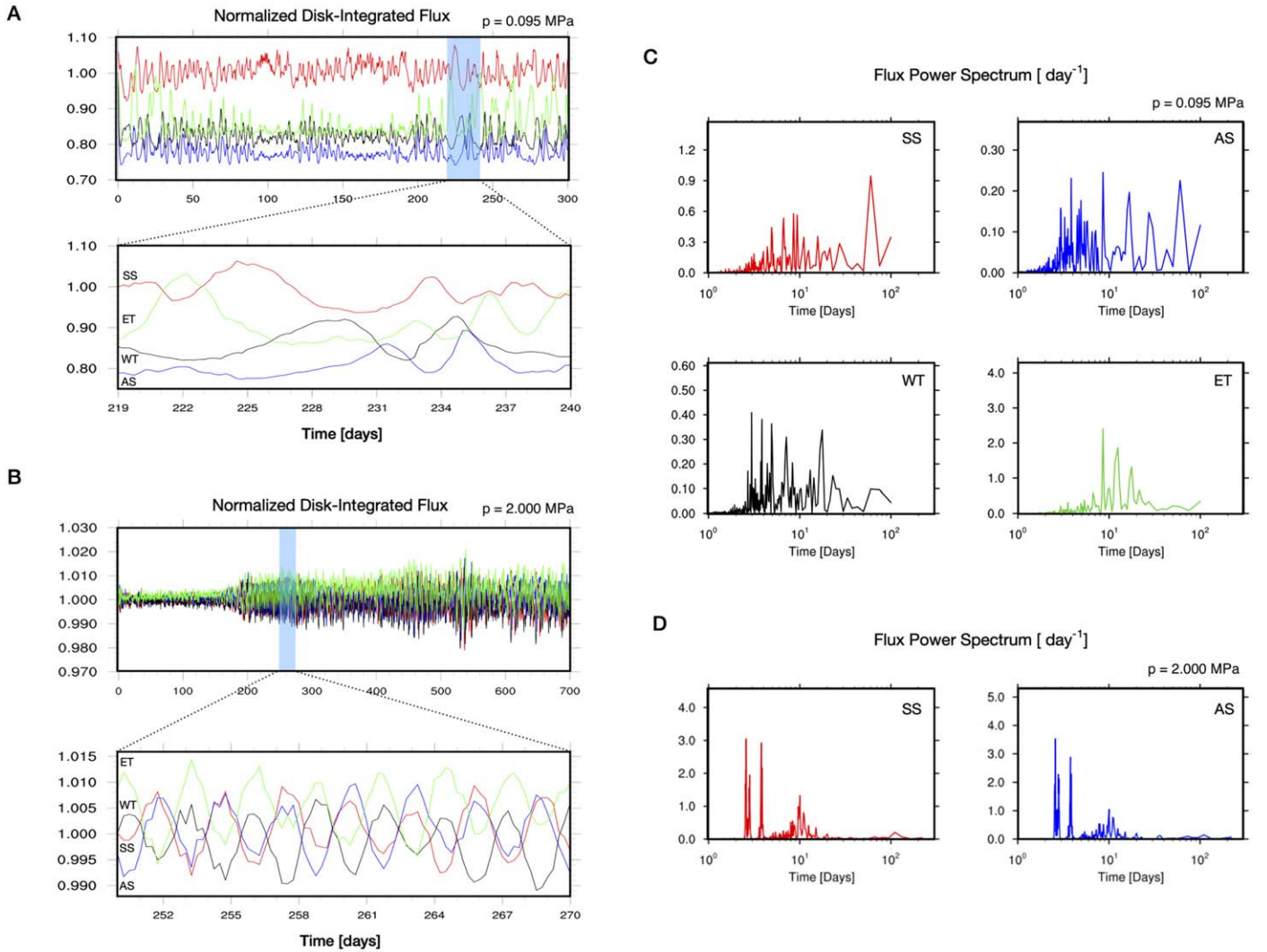
Figure 4. The time series (A, B) and power spectrum (C, D) of the disk-averaged fluxes from the fields in Figure 3. The averages are computed over disks centered at substellar (SS), antistellar (AS), eastern terminator (ET), and western terminator (WT) longitudes at the equator and normalized by their initial values at the 0.095 MPa (A) and 2.000 MPa (B) pressure levels; the insets are magnifications of the periods shaded in blue. Multiple states are seen at both levels. In (A), the four fluxes can differ by ∼30% among them as well as within a single series; in (B), the variance and the amplitudes are much smaller than at the lower pressure level, but they jump to a new state with 5 times the old values at $t \approx 180$. The hottest and coldest regions on the planet vary greatly in space and time at both levels shown. The power spectra at the two levels are correspondingly different: the spectra in (C) are broad and densely peaked, while the spectra in (D) contain few dominant peaks, indicating a much more regular pattern. The spectra for WT and ET are essentially same as in (D) at 2.000 MPa (not shown).

ET advects cold air to the dayside from the nightside. By this time, the hottest area is again near the SS point, but the coldest area is not the AS point. At $t = 105$, the whole cycle has begun again, with the hottest region ∼30° east of the SS point. The period of this particular cycle is ∼17 τ.

In contrast, entirely different states are seen in Figures 3(B) and (C). In Figure 3(B), rather than translating as a coherent structure, the cyclonic modon (in this cycle) is in a "flapping state": the northern and southern hemispheric halves alternately "spin out"—transporting heat to higher latitudes in both hemispheres in a periodic, sinuous manner. The period of this cycle is ∼3 τ. Note that the two states in Figures 3(A) and (B) can switch back and forth many times throughout the simulation. In the deep part of the atmosphere (Figure 3(C)), modons that initially formed at early times can arrange themselves into a quartet of storms, often translating together westward in a von Kármán vortex street–like configuration. Here the temperature variation and flow speed are comparatively smaller than those in the upper part of the atmosphere,

but they are no less dynamic—and, importantly, much more periodic (with dominant periods of ∼2.5 τ and ∼5 τ). Due to the slower speed in the deep region, the flow is geostrophic; hence, hot and cold regions are generally very tightly associated with anticyclones and cyclones, respectively. Note also that thermal forcing is not applied at pressure levels ⩾1 MPa (Liu & Showman 2013; Cho et al. 2015); hence, the temperature variations are directly caused by the storms, which are entirely powered by the much more vigorous activity at the lower pressure levels (Figure 1).

All of these different states produce a distinct signature in the disk-averaged temperature flux. Figure 4 shows the behavior of the atmosphere over long durations. Time series of the disk-averaged flux (proportional to T^4 and adjusted for the surface normal orientation)[8] from the simulations presented in Figure 3 are shown in Figures 4(A) and (B), where a set of four series

---

[8] Without radiative transfer, cloud, and other ingredients for additional physical realism, T^4 is an adequate measure of the equilibrium flux.

are shown for each pressure level. The averages are obtained, centered at four key points on the planet: SS, AS, ET, and western terminator (WT). Each set of temperature fluxes are normalized by the initial mean value at the indicated pressure level; the insets show the magnifications of the periods shaded in blue, illustrating the clear in-phase and "out-of-phase" nature of the hot and cold "spots" over the planet. The period power spectra of the corresponding times series in Figures 4(A) and (B) are also shown in Figures 4(C) and (D), respectively. Note, the power spectra for WT and ET (not shown) are nearly identical to those for SS and AS in Figure 4(D), the latter two of which are themselves essentially identical to each other. This is as expected from the simple translation behavior in Figure 3(C); in general, slight variations are observed as the quartet of storms transitions to other configurations (not shown).

Such multiple states are readily seen at both pressure levels (Figures 4(A) and (B)). Although the states are generally different at different levels, periodic states are present over long durations at all levels. However, the time series at higher pressure levels often undergo state transitions correlated with transitions at lower pressure levels, usually after a time delay—e.g., the transition to higher amplitude-variance flux state at $t \approx 180$ in Figure 4(B) "kicking in" following energetic activity at Figure 4(A) (cf. ET series in Figures 4(A) and (B), upper panels, starting at $t \approx 120$). This helps to establish a quasi-barotropic structure over the whole atmosphere. We stress here that, despite the slower flow speed and smaller temperature flux variation (compared to those at the lower pressure levels), the flow *before* the transition is also quite active at the higher pressure level; thus, temperature (and species) mixing occurs at the higher pressure level, even at this stage of the evolution when the fields appear nearly "quiescent." Note that, at the higher pressure level, the fluxes can be very roughly divided into two groups according to their amplitudes ({SS, AS} and {ET, WT}), in contrast to those at the lower pressure level (Figures 4(A) and (B), lower panels). Hence, global temperature oscillations are not vertically (radially) aligned.

Consistent with the time series, while the four power spectra at the lower pressure level share common peaks, the spectra are all very distinct (Figure 4(C)). This is in marked contrast to the spectra at the higher pressure level (Figure 4(D)). The spectra at the lower pressure level are broad and densely peaked, but the spectra at the higher pressure level essentially exhibit few peaks, with prominent ones at $t \sim 2.5$, $t \sim 3.8$, and $t \sim 10$. This is consistent with the four series at the higher pressure level, which are essentially just shifted in phase (Figure 4(B)). Note also that, at this pressure level, although there is a jump in flux variance at $t \approx 180$, the $\sim 2.5\,\tau$ period does not change before and after the jump. However, period shifts within a state do occur, in general, manifested as new peaks in the spectra; for example, $\sim 5.5\,\tau$ and $\sim 8.5\,\tau$ periods before the jump gradually shift to $\sim 3.8\,\tau$ and $\sim 10\,\tau$ periods (Figure 4(D)), respectively, after $t \sim 300$. Thus, some peaks remain constant across states, and some peaks slowly change within a state.

4. Discussion

When the dynamics is adequately resolved over the required range of scales for hot Jupiters, our simulations show that intense storms induce variability on the global scale—including causing hot and cold "spots" to be located both eastward and westward of the SS and AS points, respectively, at different

times. Here we have used a setup (thermal forcing and initial-boundary condition) which is commonly used in current extrasolar planet studies, in order to focus on robust dynamics. Quantitative aspects of the storms, variability, and states may change depending on the precise setup and resolution used (Thrastarson & Cho 2010; Cho et al. 2015). Hence, further investigations of the dependence on the setup—at high resolution—should be carried out for increased accuracy. Based on the numerical accuracy and convergence of the obtained solutions (Polichtchouk et al. 2014; Skinner & Cho 2021a), the features reported here are qualitatively robust and should apply generically to all 1:1 spin–orbit synchronized planets, including telluric ones. Storms undergo transitions to and from different persistent states or remain in one state over long periods, producing flux signatures that may be observable.

ORCID iDs

James Y-K. Cho ⓘ https://orcid.org/0000-0002-4525-5651
Jack W. Skinner ⓘ https://orcid.org/0000-0002-5263-385X
Heidar Th. Thrastarson ⓘ https://orcid.org/0000-0003-1041-0604

References

Armstrong, D., de Mooij, E., Barstow, J., et al. 2016, NatAs, 1, 4
Bell, T., Zhang, M., Cubillos, P., et al. 2019, MNRAS, 489, 1995
Boyd, J. P. 2000, Chebyshev and Fourier Spectral Methods (New York: Dover)
Cho, J. Y-K., Menou, K., Hansen, B. M. S., & Seager, S. 2003, ApJ, 587, L117
Cho, J. Y-K., Menou, K., Hansen, B. M. S., & Seager, S. 2008, ApJ, 675, 817
Cho, J. Y-K., Polichtchouk, I., & Thrastarson, H. Th. 2015, MNRAS, 454, 3423
Cho, J. Y-K., & Polvani, L. M. 1996, PhFl, 8, 1531
Cho, J. Y-K., Thrastarson, H. Th., Koskinen, T. T., et al. 2019, in Zonal Jets: Phenomenology, Genesis, and Physics, ed. B. Galprin & P. L. Read (Cambridge: Cambridge Univ. Press), 550
Crossfield, I. J. M., Hansen, B. M. S., Harrington, J., et al. 2010, ApJ, 723, 1436
Dobbs-Dixon, I., & Agol, E. 2013, MNRAS, 435, 3159
Fromang, S., Leconte, J., & Heng, K. 2016, A&A, 591, A144
Goldreich, P., & Soter, S. 1966, Icar, 5, 375
Grillmair, C. J., Burrows, A., Charbonneau, D., et al. 2008, Natur, 456, 767
Heng, K., Menou, K., & Phillipps, P. J. 2011, MNRAS, 413, 2380
Jackson, B., Adams, E., Sandidge, W., et al. 2019, AJ, 157, 239
Knutson, H. A., Charbonneau, D., Allen, L. E., et al. 2007, Natur, 447, 183
Komacek, T. D., & Showman, A. P. 2020, AJ, 888, 2
Lahaye, N., & Zeitlin, V. 2012, JFM, 706, 71
Liu, B., & Showman, A. P. 2013, ApJ, 770, 42
Mayne, N. J., Baraffe, I., Acreman, D. M., et al. 2014, A&A, 561, A1
Mendonça, J. M., Grimm, S. L., Grosheintz, L., & Heng, K. 2016, ApJ, 829, 115
Menou, K. 2020, MNRAS, 493, 5038
Penn, J., & Vallis, G. K. 2017, ApJ, 842, 101
Polichtchouk, I., & Cho, J. Y-K. 2012, MNRAS, 424, 1307
Polichtchouk, I., Cho, J. Y-K., Watkins, C., et al. 2014, Icar, 229, 355
Rauscher, E., & Menou, K. 2010, ApJ, 714, 1334
Scott, R. K., Rivier, L., Loft, R., & Polvani, L. M. 2004, NCAR Technical Note No. 456
Seager, S., Richardson, L. J., Hansen, B. M. S., et al. 2005, ApJ, 632, 1122

Showman, A. P., Fortney, J. J., Lian, Y., et al. 2009, ApJ, 699, 564
Showman, A. P., & Guillot, T. 2002, A&A, 385, 166
Showman, A. P., & Polvani, L. M. 2011, ApJ, 738, 71
Skinner, J. W., & Cho, J. Y-K. 2021a, MNRAS, 504, 5172
Skinner, J. W., & Cho, J. Y-K. 2021b, MNRAS, submitted
Stern, M. E. 1975, JMR, 33, 1

Swain, M. R., Vasisht, G., & Tinetti, G. 2008, Natur, 452, 329
Thrastarson, H. Th., & Cho, J. Y-K. 2010, ApJ, 716, 144
Thrastarson, H. Th., & Cho, J. Y-K. 2011, ApJ, 729, 117
Tsai, S.-M., Dobbs-Dixon, I., & Gu, P.-G. 2014, ApJ, 793, 141
von Essen, C., Stefansson, G., Mallonn, M., et al. 2019, A&A, 628, A115
Watkins, C., & Cho, J. Y-K. 2010, ApJ, 714, 904